Journal of The Electrochemical Society, 2020 **167** 110550
1945-7111/2020/167(11)/110550/10/$40.00 © 2020 The Electrochemical Society ("ECS"). Published on behalf of ECS by IOP Publishing Limited

Anisotropic Elastic Properties of Battery Anodes

Kyle S. Nagy[1] **and Donald J. Siegel**[1,2,3,4,z]

[1]*Mechanical Engineering Department, University of Michigan, Ann Arbor, Michigan 48109, United States of America*
[2]*Materials Science and Engineering, University of Michigan, Ann Arbor, Michigan 48109, United States of America*
[3]*Applied Physics Program, University of Michigan, Ann Arbor, Michigan 48109, United States of America*
[4]*University of Michigan Energy Institute, University of Michigan, Ann Arbor, Michigan 48109, United States of America*

Negative battery electrodes based on metals exhibit theoretical energy densities that surpass those of the intercalation-based anodes used in present-day Li-ion batteries. Nevertheless, metal anodes have a propensity to form dendrites during charging; thus, use of interfacial protection schemes or solid electrolytes (SE) may be necessary for these systems to be practical. The efficacy of these schemes are influenced by the interplay of the mechanical properties of the anode with those of the SE. To aid in the design of robust anode/SE interfaces, the present study employs Density Functional Theory calculations to assess the elastic properties of eight candidate anode materials: Li, Na, K, Ca, Mg, Zn, Al, and Si. The elastic constants, Young's modulus, and shear modulus are predicted as a function of temperature within the quasi-harmonic approximation. Anisotropy is assessed by resolving the moduli as a function of crystallographic direction. The alkali metals (Li, Na, and K) are predicted to have the smallest elastic moduli overall, and their moduli decrease with increasing atomic number. Regarding anisotropic behavior, Al and Mg are predicted to exhibit highly isotropic elastic properties, while the alkali metals are highly anisotropic. In the cubic systems, the crystallographic directions exhibiting extrema in the elastic properties are diametrically opposed: under axial loading the stiffest (most compliant) orientation is ⟨111⟩ (⟨100⟩), while in shear ⟨100⟩ (⟨111⟩) is the stiffest (most compliant). Importantly, the maximum anisotropic shear modulus of some metals is observed to be more than twice as large as their respective polycrystalline values. In these cases the polycrystalline properties may be a poor approximation to the elastic behavior. Accounting for this anisotropy, the resistance to dendrite initiation of several classes of solid electrolytes is discussed.
 [DOI: 10.1149/1945-7111/aba54c]

Manuscript submitted May 14, 2020; revised manuscript received June 26, 2020. Published July 23, 2020.

Supplementary material for this article is available online

The energy density of Li-ion batteries is superior to that of other secondary batteries. Nevertheless, the capabilities of the Li-ion chemistry is approaching its limits.[1] Stringent demands imposed on the energy storage system in emerging applications such as electric vehicles suggest that alternative battery chemistries with enhanced energy densities are highly desirable.[1–3]

Today's Li-ion batteries employ carbon-based anodes that operate via Li-intercalation. Anodes based on metals or silicon offer much greater gravimetric and volumetric energy densities.[4,5] Substituting these materials for today's intercalation materials presents a pathway towards improved electrochemical energy storage devices.

To be practical as a rechargeable battery electrode, a metal anode should allow for electrodeposition processes (during charging) that avoid dendrite formation over hundreds to thousands of cycles. For nearly all metal anode systems, this goal remains unmet.[5] Li metal was initially used as the anode in the earliest rechargeable Li batteries, but ensuring safe operation, including internal short circuiting from Li dendrites, proved challenging.[6] Similarly, Zn anodes cycled in alkaline electrolytes exhibit dendrite formation.[7,8] Rechargeable batteries utilizing Na, including Na-ion, Na-O_2, and Na-S, have been the subject of on-going interest,[9–11] but, like Li, metallic Na is also susceptible to dendrite formation during cycling.[11] Ren et al. demonstrated a K-O_2 cell, but did not characterize dendrite formation during a small number of cycles.[12] Zhao et al. reported a K-S battery where no dendrites were reported after 50 cycles.[13] Anodes based on Al have long been known to readily form dendrites during plating from molten salt solutions.[14] Strategies to overcome this issue have met with mixed results.[15] For example, a cell consisting of an Al anode, a pyrolytic graphite foil, and $AlCl_3$/1-ethyl-3-methylimidazolium chloride [EMIm]Cl electrolyte recently demonstrated dendrite-free cycling.[16] Cycling of a Ca metal anode, long thought impossible,[17] was recently achieved with $Ca(BH_4)_2$ in tetrahydrofuran (THF) at room temperature, where Ca metal films free of dendritic deposits were reported.[18] Matsui performed extensive cycling of Mg anodes in a Grignard-based electrolyte, and reported granular deposits.[19] More recent work on Mg batteries has shown that dendrites can also form in this system.[20]

The propensity for metallic anodes to form dendrites during charging implies that the use of interfacial protection schemes or solid electrolytes (SE) may be necessary for these systems to be practical. In principle, a stiff and dense SE could prohibit dendrite initiation simply by pressing against the anode. The pressure applied by the SE is expected to inhibit inhomogeneous metal deposition and the protrusions (i.e. dendrite nuclei) that would result.[21] This hypothesis has sparked interest in understanding the mechanical properties of the anode, the SE, and their interfacial region. For example, Monroe and Newman proposed a relationship between a SE's elastic properties and its ability to mitigate dendrites.[22] To suppress the formation of surface protrusions (i.e., dendrite nuclei) on the anode, their model suggested that the ratio of the shear modulus of the SE to that of the anode should be greater than approximately two.

Nevertheless, numerous examples exist of lithium metal-based cells undergoing failure due to dendrite formation.[23–30] These failures have been observed at relatively low current densities (0.2 mA cm^{-2}) and in cells using solid electrolytes possessing shear moduli far in excess of that for Li (∼4.25 GPa).

These observations suggest that mechanical phenomena beyond (or in combination with) the elastic regime may be important in understanding the failure of solid state batteries. Consequently, other mechanical properties related to the anode, solid electrolyte, and their interfaces have been topics of recent interest. For example, Barai et al. developed a model of the metal/SE interface that included the effects of plastic deformation.[31] They concluded that increasing the yield strength of the solid electrolyte can stabilize metal deposition, even if the SE's elastic modulus is significantly lower than the Monroe and Newman criterion. Other work has explored the role of pressure,[32] the possibility for increased mechanical strength at small sizes,[33–39] electrochemically activated mechanisms such as 'grain coating,'[40] stress accumulation at the electrode/SE interface and at defects in the SE,[30] creep within the anode,[41–43] and softening at grain boundaries.[44]

To aid in the design of robust solid electrolyte/metal anode interfaces, as well as to inform strategies for implementing Si-based anodes, the present study employs first-principles calculations to

[z]E-mail: djsiege@umich.edu

evaluate the elastic constants and aggregate, polycrystalline elastic properties of 8 next-generation anode materials, including Al, Ca, Li, Na, K, Mg, Zn, and Si. Based on the calculated elastic constants, the anisotropic Young's moduli and shear moduli are derived. Additionally, the effects of temperature on these elastic properties are evaluated at 150 K, 300 K, and 450 K using the quasi-harmonic approximation.[45] Accurate predictions of the elastic properties are shown to require careful convergence of the elastic constants with respect to the density of the k-point grid. Prior first-principles calculations have successfully predicted the elastic constants for metals,[46–48] Si,[49] and alloys.[50,51]

In general, excellent agreement between the present calculations and experimental measurements is obtained for the elastic constants and polycrystalline elastic moduli. The calculated elastic properties are mapped as a function of crystallographic direction. Extrema in these properties are identified under axial and shear loading. Interestingly, in the cubic systems the locations of these extrema are diametrically opposed: under axial loading the stiffest (most compliant) orientation is ⟨111⟩ (⟨100⟩), while in shear ⟨100⟩ (⟨111⟩) is the stiffest (most compliant).

The alkali metals (Li, Na, and K) are found to be the softest metals overall, with softness increasing with atomic number. The alkali metals are also the most anisotropic, and, unlike the other elements examined here, the degree of anisotropy of the alkali metals increases with increasing temperature. A larger degree of anisotropy implies that the mechanical properties of these metals will vary more significantly with orientation, potentially resulting in different likelihoods for dendrite formation/growth at the anode/SE interface. In contrast, Al and Mg are the most isotropic metals examined; their elastic properties are more sensitive to temperature than for the other elements studied here. Si, the only non-metal, is the stiffest overall.

Based on the criterion of Monroe and Newman, the present calculations suggest that the thiophosphates are only appropriate as a solid electrolyte in conjunction with anodes based on K. In the case of anti-perovskite-based SE's, anodes based on alkali metals (Li, Na and K) would satisfy the MN criterion, while NASICON-type and garnets further expand the number of suitable anode compositions to include Ca and Mg in addition to the alkali metals. Perovskite SEs satisfy MN for all anode compositions studied here except Si. In sum, the directionally-resolved and temperature-dependent elastic properties reported here will be of value in the construction of mechano-electrochemical models of phenomena at metal/solid electrolyte interfaces.

Methods

Density functional theory calculations[52] were performed using the Vienna ab-initio Simulation Package (VASP).[53–56] Blöchl's projector augmented wave method[57] (PAW) was used to describe the interaction of core and valence electrons, and a conjugate-gradient algorithm with corrector steps was used to relax the ion positions. For the metallic systems, orbital occupancies were determined using the Methfessel–Paxton method[58] with a smearing width of 0.1 eV; a Gaussian-type method with a sigma value of 0.1 eV was used for Si. The electronic self-consistency iterations were terminated when the change in total energy and the change in electronic eigenvalues were both less than 10^{-7} eV. Hellmann-Feynman forces were converged to within 0.005 eV $Å^{-1}$.

The plane-wave cutoff energies used for Al, Ca, Li, Na, K, Mg, Zn, and Si were 400 eV, 300 eV, 300 eV, 250 eV, 360 eV, 300 eV, 610 eV, and 420 eV, respectively. Extremely dense k-point sampling mesh densities were employed, with respective values of 40^3, 19^3, 49^3, 44^3, 27^3, 40^3, 37^3, and 14^3. These densities often exceed those used in prior studies; for example, in the Dryad data repository, de Jong et al.[59,60] used grids of size 45000 ($\sim 35^3$) for Al, 20000 ($\sim 27^3$) for Li and Na, and 7000 ($\sim 19^3$) for K, Ca, Mg, Zn, and Si. Our tests confirm that thorough k-point sampling is necessary for achieving converged elastic properties, as illustrated in Fig. S1 (available online at stacks.iop.org/JES/167/110550/mmedia). Further details regarding the convergence behavior of the elastic properties with respect to the plane-wave cutoff energy and k-point sampling are provided in the Supporting Information.

A total of 5 exchange-correlation functionals were evaluated for each element by comparing the calculated elastic constants with experimental data measured at absolute zero, or at low temperatures approaching 0 K. The results of these tests are summarized in Table SII. The exchange-correlation functional of Perdew–Burke–Ernzerhof[61] (PBE) was determined to most closely match experimental data, and was therefore used for the remainder of the study.

The stiffness matrix was calculated via a stress-strain relationship.[62] Three axial and three shear strains of ±1% of the lattice vector were applied to the unit cell, and the resulting stresses were calculated. The elements of the stiffness matrix, C_{ij}, were derived from a series of linear least-squares fits to this stress-strain data. Example stress-strain curves are shown in Fig. S18. The compliance matrix, S_{ij}, was calculated as the inverse of the stiffness matrix. It should be noted that the value that VASP reports as C_{44} is defined by Nye[63] as the C_{66} stiffness coefficient; Nye's convention is used for all elastic properties discussed hereafter.

Several elastic properties were calculated from the elements of the compliance and stiffness matrices. The bulk and shear moduli of aggregated, polycrystalline materials as defined by Voigt, Reuss, and Hill[64] were calculated according to

$$B_{Voigt} = \frac{C_{11} + C_{22} + C_{33} + 2(C_{12} + C_{23} + C_{31})}{9}$$
$$B_{Reuss} = \frac{1}{S_{11} + S_{22} + S_{33} + 2(S_{12} + S_{23} + S_{31})}$$
$$B_{Hill} = \frac{B_{Voigt} + B_{Reuss}}{2} \quad [1]$$

$$G_{Voigt} = \frac{C_{11} + C_{22} + C_{33} - (C_{12} + C_{23} + C_{31}) + 3(C_{44} + C_{55} + C_{66})}{15}$$
$$G_{Reuss} = \frac{15}{4(S_{11} + S_{22} + S_{33}) - 4(S_{12} + S_{23} + S_{31}) + 3(S_{44} + S_{55} + S_{66})}$$
$$G_{Hill} = \frac{G_{Voigt} + G_{Reuss}}{2} \quad [2]$$

from which the Voigt, Reuss and Hill elastic moduli and Poisson ratios were calculated as

$$E = \frac{9BG}{3B + G}, \nu = \frac{3B - 2G}{2(3B + G)} \quad [3]$$

Anisotropic elastic properties were also calculated from the stiffness and compliance matrices. For comparison, the amount of elastic anisotropy was determined using the Universal Anisotropy index (A^U),[65]

$$A^U = 5\left(\frac{G_{Voigt}}{G_{Reuss}}\right) + \left(\frac{B_{Voigt}}{B_{Reuss}}\right) - 6 \quad [4]$$

for which a value of 0 indicates perfect isotropy, and a larger value indicates greater anisotropy. The anisotropic Young's[63] and shear[66] moduli are given, respectively, as

$$E(a_1, a_2, a_3)^{-1} = S_{11}{a_1}^4 + S_{22}{a_2}^4 + S_{33}{a_3}^4 + (2S_{12} + S_{66}){a_1}^2{a_2}^2 + (2S_{23} + S_{44}){a_2}^2{a_3}^2 + (2S_{13} + S_{55}){a_1}^2{a_3}^2 \quad [5]$$

$$G(a_1, a_2, a_3, b_1, b_2, b_3)^{-1} = 4(S_{11}{a_1}^2{b_1}^2 + S_{22}{a_2}^2{b_2}^2 + S_{33}{a_3}^2{b_3}^2) + 8(S_{12}a_1b_1a_2b_2 + S_{23}a_2b_2a_3b_3 + S_{13}a_1b_1a_3b_3) + S_{44}(a_2b_3 + a_3b_2)^2 + S_{55}(a_1b_3 + a_3b_1)^2 + S_{66}(a_1b_2 + a_2b_1)^2 \quad [6]$$

Here, $\vec{a}$ is a vector that points radially from the origin, and represents a vector normal to a surface on a crystal that is centered at the origin. Vector $\vec{b}$ is perpendicular to $\vec{a}$, as indicated in Fig. 1, and represents the direction of a shear stress parallel to the surface that is normal to $\vec{a}$. The Cartesian components of these vectors are defined as:

$$\begin{aligned} a_1 &= \cos\phi\cos\theta \\ a_2 &= \cos\phi\sin\theta \\ a_3 &= \sin\phi \\ b_1 &= \sin\phi\cos\theta\cos\chi - \sin\theta\sin\chi \\ b_2 &= \sin\phi\sin\theta\cos\chi + \cos\theta\sin\chi \\ b_3 &= -\cos\phi\cos\chi \end{aligned} \quad [7]$$

The angles θ and φ are the polar and azimuthal angles, respectively, while χ defines the direction of the shear, given by $\vec{b}$.

The effect of temperature on the calculated elastic properties was evaluated within the quasi-harmonic approximation[67] (Phonopy code).[68] Equilibrium volumes were calculated at three temperatures: 150 K, 300 K, and 450 K. Using the previously-mentioned stress-strain relationship, elastic constants at these temperatures were calculated using the expanded lattice volumes predicted by the quasi-harmonic calculations (Table SIII). Following the procedure outlined in Ref. 45 static energy contributions to the free energy were assumed to be dominant, thus allowing for the vibrational free energy and thermal electronic free energy contributions to be neglected; hence the primary impact of finite temperatures on the elastic properties is assumed to arise from thermal expansion or contraction of the lattice.[45]

Results and Discussion

Elastic constants.—Emphasis was placed on achieving converged predictions with respect to sampling of the Brillouin zone (i.e., k-point sampling). The more complex Fermi surface of metals generally requires denser k-point sampling than for materials with a band gap (semi-conductors and insulators). These sampling requirements are further compounded by the lattice strains needed to evaluate elastic constants; these strains lower the symmetry of the Brillouin zone, thereby increasing the number of symmetry-distinct k-points that must be sampled. Finally, materials with small elastic constants, such as the alkali metals, present additional challenges to achieving convergence. For example, in the case of lithium, use of an insufficient k-point mesh results in an elastic tensor that is not positive definite, and therefore violates the Born stability conditions.[59,60,69,70] (See Fig. S1).

Calculated elastic constants for the eight elements examined in this work are summarized in Table I. The cubic elements, (Al, Ca, Li, Na, K, and Si) possess three independent elastic constants, C_{11}, C_{12}, and C_{44}, while the elements with hexagonal close-packed crystal structures, Mg and Zn, possess two additional independent elastic constants, C_{13} and C_{33}. The elastic constants are calculated for three temperatures, 150 K, 300 K, and 450 K, using the lattice constants determined for each temperature from the quasi-harmonic approximation. The elastic constants and elastic properties of Na and K were not calculated at 450 K because this temperature exceeds their melting temperatures (371 K and 337 K, respectively). As expected, in all cases the elastic constants decrease as the temperature increases.[71] Table SIII presents a comparison between the calculated and experimental lattice constants as a function of temperature.

Overall, very good agreement is achieved between the calculated and experimentally measured elastic coefficients. The PBE functional, which was observed to be the most accurate functional out of those examined, yields an average error of 8.6% at low temperatures, Table SII. (See Table SIV for a summary of experimental data at 150 K, 300 K, and 450 K). Deviations between the experimental data and the values calculated here are also summarized in Table I. The calculations on Al exhibit the best agreement with experiments, with deviations across all temperatures of less than 10%. The calculated values for Si, Ca, Li, Na, K, and Mg deviate from experiment by 3%–18% across all temperatures, with the size of the deviation increasing with temperature. (One exception is Na, which has a greater difference at 0 K than at 150 K). It should be noted that the alkaline metals (Li, Na, and K) have small elastic coefficients which tend to inflate the deviation percentages reported in Table I. Disagreement between the calculated and experimental coefficients is greatest for Zn, ranging from 22.7%–44.2%; the variation in the elastic constants with temperature for Zn is also much greater than for the other materials. Nevertheless, the Born stability requirements for Zn are satisfied at all temperatures, and the 0 K values calculated by other authors[59] are consistent with the values reported here (Table SII). Table SIV shows that a relatively large standard deviation exists in the experimental elastic constant data for Zn.

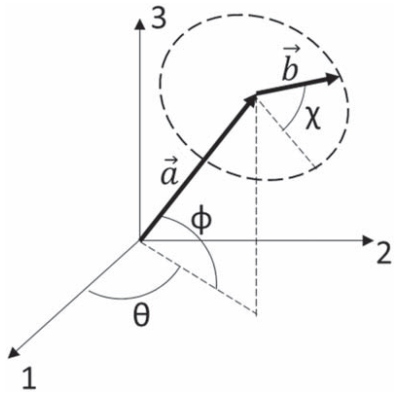

Figure 1. Coordinate system for evaluation of directionally-resolved elastic properties. $\vec{b}$ is anti-parallel to $\vec{3}$ when $\chi = \phi = 0°$.

Isotropic elastic properties.—Figure 2 summarizes the calculated isotropic elastic properties, as determined using Eqs. 1–3 and the elastic coefficients in Table I. These data indicate that the alkali metals generally have the smallest values of these moduli (i.e., are the softest), followed in order of increasing stiffness by Ca, Mg, Zn, Al, and Si. The values of the moduli for Li, Na, K, Ca, and Si show little change with temperature, while Mg, Al, and Zn exhibit greater sensitivity to temperature. As with the elastic constants, there is generally excellent agreement between experiments and the calculated isotropic values for E and G (see Tables I, SV, and SVI). With the exception of Si and Zn, deviations are on the order of a few GPa. For Si, deviations range from 7%–9%, and 33%–79% for Zn.

To place these values in context, it is helpful to compare with the experimental Young's modulus for several solid electrolytes. These moduli vary widely across the different SE classes: 10–100 MPa for polymers,[72,73] 17–36.9 GPa for alkaline thiophosphates,[74–76] 77 GPa for LiPON,[77] 57.4–99.7 GPa for alkaline anti-perovskites,[76,78] 115–143.7 GPa for NASICON,[76,79] 140–175.1 GPa for garnets,[76,79,80] and 143–262.5 GPa for perovskites.[76,79] With the exception of the polymer-based systems, all of these SE classes exhibit values for E that are larger than those calculated for alkali metal anodes.

Anisotropic Young's moduli.—Figure 3 plots the anisotropic behavior (i.e., directional dependence) of the Young's and shear moduli at 300 K. Here, solid bars represent the minimum values of the modulus, and the hatched bars represent the difference between the maximum and minimum values. The length of the hatched bar relative to the length of the entire bar reflects the amount of anisotropy, which is quantified by A^U, and listed in Table I. These data show that Al is the most isotropic element considered here, having $A^U = \sim 0$. In contrast, the alkali metals (A^U = 6 to 13) and Zn (A^U = 4 to 27) exhibit significant anisotropy in their elastic moduli. The alkaline earths and Si fall between these two extremes.

Table I. Calculated elastic constants, C_{ij} and Isotropic Elastic Properties (in GPa), as a function of temperature. For comparison, experimental values within 3 ("Expt: 300 ± 30").[a)]

	Temp. (K)	C_{11}	C_{12}	C_{13}	C_{33}	C_{44}	% error	B	E
Al	150	112.5	55.0			29.8	9.6	74.2	77.9
	300	108.8	53.0			28.4	8.0	71.6	74.8
	Expt: 300 ± 30	108 ± 2.1	61.5 ± 2.1			28.3 ± 0.3		76.9 ± 2.1	70.4
	450	104.3	50.7			26.7	9.4	68.6	71.0
Ca	150	22.3	14.6			13.9		17.2	21.5
	300	21.8	14.2			13.8	13.6	16.7	21.3
	Expt: 300 ± 30	25.3 ± 2.5	17.1 ± 1.1			15.2 ± 1.2		19.8 ± 1.6	23.5
	450	21.3	13.7			13.6		16.2	21.0
Li	150	14.9	12.2			11.2	7.6	13.1	13.5
	300	14.3	11.6			11.0	15.0	12.5	13.2
	Expt: 300 ± 30	13.3 ± 0.2	11.3 ± 0.2			8.8 ± 0.1		12.0 ± 0.2	10.7
	450	13.6	11.0			10.7		11.9	12.8
Na	150	7.9	6.9			5.9	7.7	7.2	6.5
	300	7.1	6.3			5.5	18.1	6.6	6.0
	Expt: 300 ± 30	6.3 ± 0.9	5.1 ± 0.9			4.8 ± 0.8		5.5 ± 0.9	5.8 ±
K	150	3.8	3.0			2.5	8.3	3.3	3.3
	300	3.4	2.8			2.4	10.1	3.0	3.0
	Expt: 300 ± 30	3.8 ± 0.4	3.2 ± 0.1			2.3 ± 0.4		3.4 ± 0.2	2.7 ±
Mg	150	60.9	22.6	17.9	59.7	19.2	10.8	33.1	46.1
	300	56.1	20.7	16.8	54.4	17.7	13.6	30.6	42.2
	Expt: 300 ± 30	58.9 ± 1.0	25.4 ± 1.0	21.0 ± 1.2	61.1 ± 1.0	16.5 ± 0.2		34.8 ± 1.1	44.6
	450	50.4	18.6	15.6	48.2	15.9		27.6	37.6
Zn	150	140.7	35.7	46.3	40.3	29.2	25.1	51.8	70.7
	300	114.3	30.8	41.0	33.7	24.3	30.1	42.9	54.9
	Expt: 300 ± 30	161 ± 8.6	30.2 ± 7.5	48.0 ± 7.1	60.7 ± 6.4	39.5 ± 0.9		64.3 ± 6.2	101 ±
	450	76.7	33.5	37.3	26.6	14.2	44.2	27.3	23.5
Si	150	150.1	53.9			73.8	11.8	85.9	150.3
	300	149.5	53.3			73.7	12.6	85.3	149.9
	Expt: 300 ± 30	166 ± 0.9	64.5 ± 0.8			80.5 ± 1.8		98.6 ± 0.9	164 ±
	450	148.4	52.2			73.4		84.3	149.2

a) $\%\ error = \sqrt{\frac{1}{n}\sum_{i=1}^{n}\left(\frac{C_{i,expt} - C_{i,calc}}{C_{i,expt}}\right)^2} \times 100$. Here, i indexes the Voigt subscripts of the elastic coefficients, and $n = 3$ for cubic systems and $n = 5$ for hexagonal sy

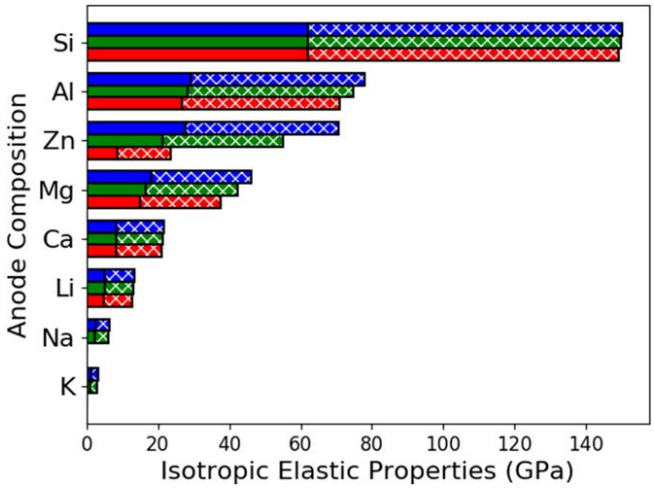

Figure 2. Variation of the isotropic elastic moduli with temperature. Differently colored bars correspond to 150 K (blue), 300 K (green), and 450 K (red). The entire bar length (solid + hatched) represents the Young's modulus, while the solid portion of the bar represents the shear modulus.

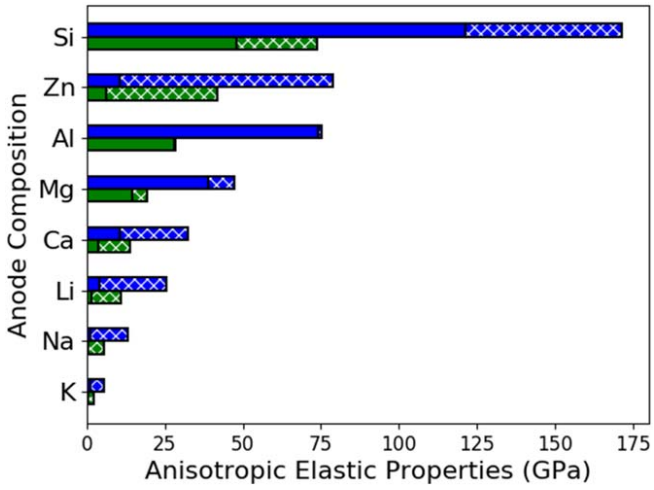

Figure 3. Anisotropy in elastic moduli. Differently colored bars correspond to the anisotropic Young's (blue) and shear (green) modulus at 300 K. The entire bar (solid + hatched) represents the maximum value, and the solid bar represents the minimum value.

Figure 4 shows the calculated Young's moduli, E, at 300 K as a function of crystallographic direction for each of the 8 elements examined. (Figs. S19 and S20 show the same data at 150 K and 450 K, respectively.) The shape of each plot indicates the degree of anisotropy in E: compact shapes such as spheres and cubes represent more isotropic behavior, while star-shaped plots suggest a greater degree of anisotropy. As expected, the degree of anisotropy implied by a given plot's shape closely matches that element's universal anisotropy index, A^U, shown in Table I. In agreement with the calculated A^U values, the data plotted in Fig. 4 indicate that the alkali metals and Zn exhibit the most anisotropy in E.

Figure 4 also shows that the elements that adopt a cubic crystal structure (Al, Ca, Li, Na, K, and Si) exhibit similar trends in the maxima and minima of E as a function of direction. For these systems the maximum Young's modulus, E_{max}, occurs in ⟨111⟩ directions, while the minimum values, E_{min}, occur along ⟨100⟩. The one exception to this trend is Al at 450 K (see Fig. S19). This deviation can be explained by the fact that Al is almost perfectly isotropic at elevated temperature; variations in E as a function of direction are minimal in Al, spanning only 0.2 GPa.

The behavior of Mg as depicted in Fig. 4 differs from the other elements. In particular, Mg is unique in that $E_{max} = 47.1$ GPa occurs in the ⟨0001⟩ direction at 300 K. Similarly, at 150 K, $E_{max} = 52.0$ GPa also occurs in the ⟨0001⟩ direction. At these temperatures, local maxima exist as an equatorial band within the basal plane, $\varphi = 0°$, $0 \leqslant \theta \leqslant 360°$, ($E = 46.2$ and 50.2 GPa at 300 and 150 K, respectively). At 450 K the value for E projected to the equatorial plane overtakes the value along ⟨0001⟩, becoming the global maximum: $E(0001) = 41.2$ GPa $< E$(equatorial) $= 41.3$ GPa. For the temperature range examined here, the minimum value for E in Mg, E_{min}, occurs in the directions defined by $\varphi \cong 45°$, $0 \leqslant \theta \leqslant 360°$.

Finally, Fig. 4 shows that the directional dependence of E for Zn is also unique, and resembles a "yo-yo" shape. E_{max} for Zn occurs in two parallel rings defined by $0 \leqslant \theta \leqslant 360°$ and $\varphi \cong \pm 67°$, $\pm 64°$, and $\pm 60°$ at 150, 300, and 450 K, respectively. E_{min} appears as a depression on the surface located along ⟨0001⟩; E also decreases as φ approaches 0. These local minima in E become more pronounced at 450 K (Fig. S19), at which point the plot resembles two cones joined at their apexes.

As noted in Ledbetter's review,[81] Zn exhibits a high degree of elastic anisotropy, in agreement with the present results. This behavior is consistent with Zn's high c/a ratio of ∼1.87 (Table SIII)—the ideal ratio being 1.63–suggesting stronger intra-basal-plane bonding than between basal planes. (The c/a ratio predicted by the present calculations at 300 K, 1.90, is in good agreement with experimental measurements). The resolved Young's modulus data shown for Zn in Fig. 4 is consistent with these trends: $E_{min} = 10.6$ GPa occurs along ⟨0001⟩, consistent with relatively weaker bonding between basal planes, while E within the basal plane, corresponding to $\varphi = 0°$ and $0° \leqslant \theta \leqslant 360°$ is much larger, 59.0 GPa.

Anisotropic shear moduli.—Figures 5 and 6 illustrate the directionally-resolved shear modulus, G, for all 8 elements at 300 K. Figure 5 plots the maximum shear modulus, G^{Max}, within a plane perpendicular to the crystallographic direction specified by $\vec{a}$. (See Eqs. 6–7 and Fig. 1). Similarly, Fig. 6 plots the minimum shear modulus, G^{Min}, applied perpendicularly to each crystallographic direction indexed by $\vec{a}$. Figures S21–S24 show the same data at 150 K and 450 K.

As was observed for the Young's moduli, the shapes of the resolved shear modulus plots indicate the degree of anisotropy. More compact shapes (e.g. spheres) indicate greater isotropy, whereas shapes with significant directional dependence indicate greater anisotropy. For example, for cubic materials, the more anisotropic G^{Max} plots resemble three orthogonal circles with common centers that intersect in ⟨100⟩ directions; the plots of G^{Min} also convey anisotropic behavior and resemble three intersecting rods parallel to ⟨100⟩ directions.

Figure 7 plots the behavior of the shear modulus within selected low-index crystallographic planes at 300 K for $0° \leqslant \chi \leqslant 360°$ (i.e., for all orientations of b within the plane {hkl} normal to $\vec{a}$ = [hkl], as shown in Fig. 1). For the cubic systems the high-symmetry planes include $\vec{a}$= {100}, {110}, and {111}. Similar plots at 150 K and 450 K are shown in Figures S25–S26; Table SVII summarizes the Young's modulus and maximum/minimum shear modulus for each orientation at 300 K.

In the case of the cubic systems, in {100} G is independent of χ and equal to the global maximum shear modulus (see Table SVIII). This is consistent with earlier analysis by Turley and Sines, where it was predicted that G does not depend on direction within these planes.[82] In contrast, the shear moduli within {110} planes vary periodically between the global maximum, located in ⟨001⟩ directions, and the global minimum G, which occur parallel to ⟨$\bar{1}$10⟩. Within the {111} planes, the values for G are nearly constant, with slight undulations; the maxima occur at 0° and 180° (⟨$\bar{1}\,\bar{1}\,\bar{1}$⟩), and the minima occur at 90° and 270° (⟨$1\bar{1}$ 0⟩).

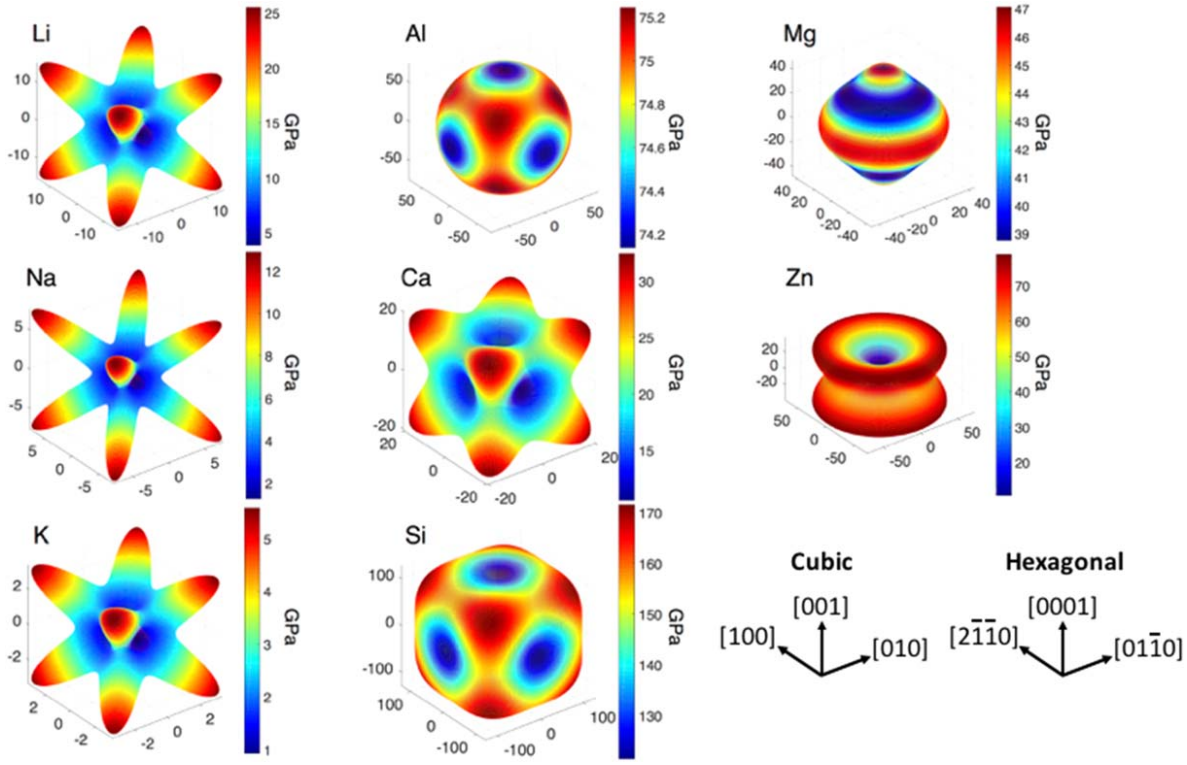

Figure 4. Calculated Young's modulus, *E*, as a function of crystallographic direction for Li, Na, K, Al, Ca, Si, Mg, and Zn at 300 K. The value of the modulus in a given crystallographic direction $\vec{a}$ is specified (redundantly) using the magnitude of the protrusion from the origin and with color coding. The range of the modulus scale varies from element-to-element. The shape of the plot indicates the degree of anisotropy: compact shapes such as cubes and spheres represent isotropic behavior; star-shaped plots suggest a greater degree of anisotropy.

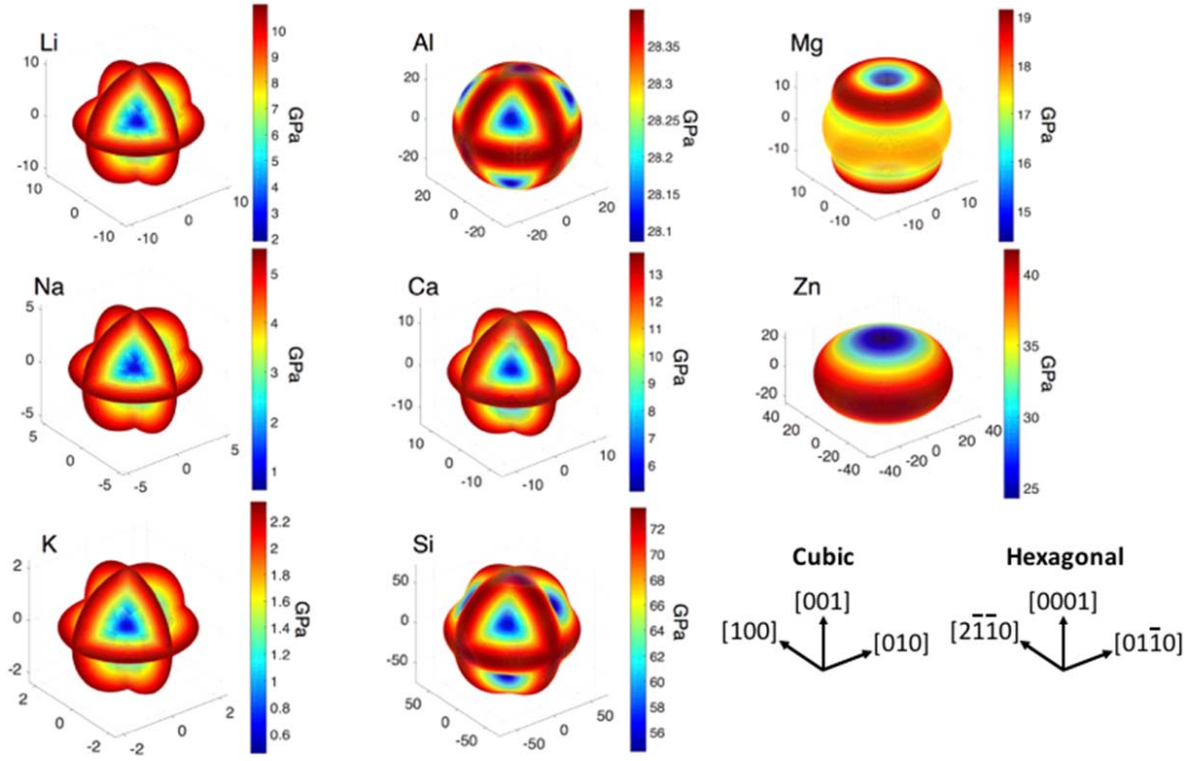

Figure 5. Calculated maximum shear modulus, G^{Max}, as a function of crystallographic direction for Li, Na, K, Al, Ca, Si, Mg, and Zn at 300 K. G^{Max} represents the maximum G over all directions $\vec{b}$ perpendicular to $\vec{a}$. The coordinate system for $\vec{a}$ is shown for cubic and hexagonal crystal structures; the relationship between $\vec{b}$ and $\vec{a}$ is shown in Fig. 1. The modulus value is specified (redundantly) using the magnitude of the protrusion from the origin and with color coding. Note that the range of the modulus scale varies from element-to-element.

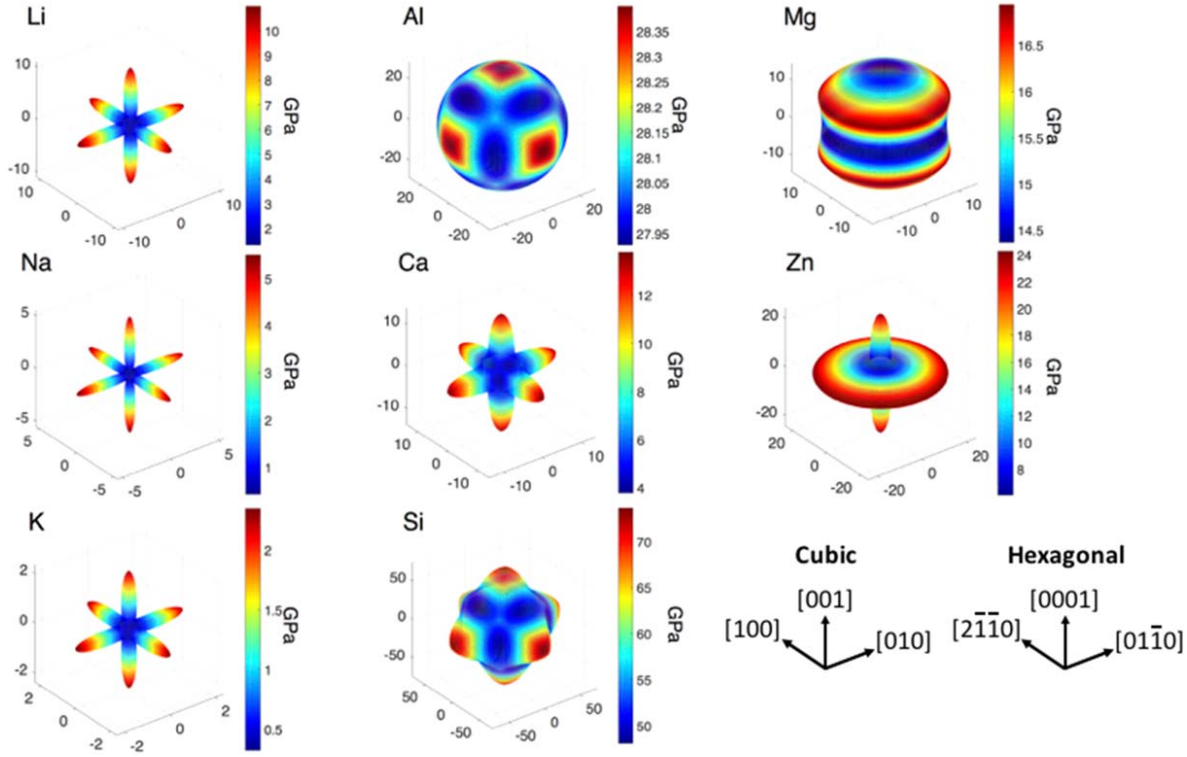

Figure 6. Calculated minimum shear modulus, G^{Min}, as a function of crystallographic direction for Li, Na, K, Al, Ca, Si, Mg, and Zn at 300 K. G^{Min} represents the smallest G for all directions $\vec{b}$ perpendicular to $\vec{a}$. The coordinate system for $\vec{a}$ is shown for cubic and hexagonal crystal structures; the relationship between $\vec{b}$ and $\vec{a}$ is shown in Fig. 1. The modulus value is specified (redundantly) using the magnitude of the protrusion from the origin and with color coding. Note that the range of the modulus scale varies from element-to-element.

In the case of hexagonal systems, Mg and Zn, the value of G within the basal plane, {0001}, is independent of χ, with (constant) values of G = 14.4 GPa for Mg, and G = 24.3 GPa for Zn. Within the prismatic planes, $\{1\bar{1}00\}$, the shear moduli for Mg oscillate between G = 17.7 GPa at 90° and 270°, and the global minimum, G_{min} = 14.4 GPa at 0° and 180°; for Zn, the oscillations occur between the global maximum, G_{max} = 41.7 GPa at 90° and 270° and G = 24.3 GPa at 0° and 180° ($\vec{b}$ is perpendicular to ⟨0001⟩ when $\chi = 0°$ or 180° for both Mg and Zn). Note that the prismatic planes occur within a continuum corresponding to $\varphi = 0°$ and $0° \leqslant \theta \leqslant 360°$, and that G^{Max} and G^{Min}, as well as G vs χ, are independent of θ within this continuum. Also plotted in Fig. 7 are G for a continuum of planes corresponding to $\varphi = \pm 45°$ and $0° \leqslant \theta \leqslant 360°$. Here, the shear moduli oscillate for Mg between G_{max} = 19.2 GPa at 0° and 180° and G = 15.9 GPa at 90° and 270°, and G = 30.7 GPa at 90° and 270° and G_{min} = 6.1 GPa at 0° and 180° for Zn.

Discussion.—Xu et al. used the quasi-harmonic approximation within density functional theory to predict the anisotropic elastic properties of Li as a function of temperature.[38] Although the present calculations are in good agreement with Xu's values for the C_{11} and C_{12} elastic constants, differences exist for C_{44} at low temperatures. More specifically, the present calculations predict a value of 11.6 GPa at 0 K (11.2 GPa at 150 K), while Xu et al. report values of 8–9 GPa. The experimentally measured value for C_{44}, 10.8 GPa at 78 K, is closer to the present results. We attribute this discrepancy to incomplete convergence of C_{44} with respect to sampling of the Brillouin zone in the Xu et al. study.[38]

The Materials Project (MP) also contains a tabulation of elastic constants for the elements considered here, as derived from DFT calculations. Compared to the MP database, the present work reports the elastic properties over a range of temperatures, whereas the data in the MP is reported only for T = 0 K. The present study also aims to achieve well-converged predictions with respect to planewave cutoff energy and k-point sampling. Consequently, the present predictions are in good agreement with the available low-temperature experimental data: Table SII demonstrates that the elastic properties predicted here are within 8.6% of experiments, whereas the data in the MP for these elements differs by 11.6% on average. Another consequence of incomplete convergence can be seen in the MP values for the potassium stiffness tensor: in violation of the Born stability criterion,[59] the MP reports $C_{12} > C_{11}$.

As was mentioned earlier, the criterion of Monroe and Newman proposes that in order to suppress dendrite initiation, the shear modulus of a solid electrolyte should be larger than that of a metallic anode placed in contact with it by a factor of approximately two. If these dendrites are crystalline, then the anisotropic elastic response of the metal should be considered, rather than the average or polycrystalline elastic properties. The data reported here demonstrate that for some metals the maximum value of the anisotropic shear modulus can be more than twice as large as the polycrystalline shear modulus. Metals that fall into this category include the alkaline metals (Li, Na, and K) and Zn. In these cases, the maximum resolved shear moduli at 300 K are 11.0 GPa, 5.5 GPa, 2.4 GPa, and 41.7 GPa, respectively, while the respective polycrystalline values are 5.0 GPa, 2.2 GPa, 1.1 GPa, and 21.3 GPa.

It is helpful to review the shear moduli of common SE classes for the purpose of evaluating their viability. These values range from: 7.9–14.1 GPa for alkaline thiophosphates,[74–76] 31 GPa for LiPON,[77] 23.6–41.5 GPa for alkaline anti-perovskites,[76,78] 47.7–57.6 GPa for NASICON,[76,79] 54.8–68.9 GPa for garnets,[76,79,80] and 91.2–104 GPa for perovskites.[76,79] In the context of the Monroe-Newman criterion and the orientation-dependent shear moduli presented here, the viability of a given SE class for a given anode composition can be projected by comparing the lower bound of the SE shear modulus (mentioned above) with twice the maximum resolved shear modulus of the anode at 300 K. Within this approximation, the thiophosphates, which are the most compliant of the SE considered, are projected to be appropriate only for use

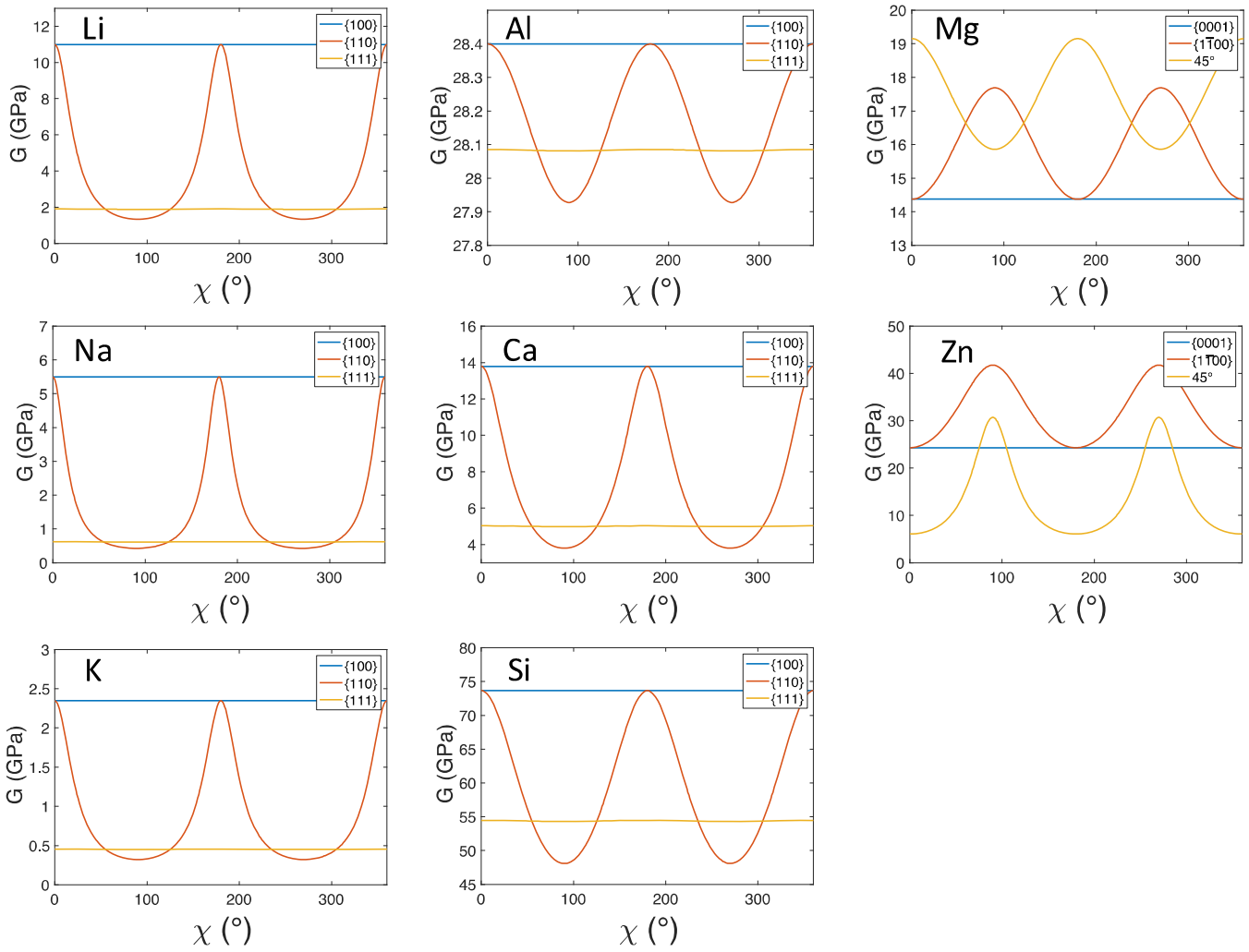

Figure 7. Variation in the shear modulus for Li, Na, K, Al, Ca, Si, Mg, and Zn at 300 K within several low-index crystallographic planes. Low-index planes for the cubic system include {100}, {110}, and {111}. χ identifies the angle of the shear direction $\vec{b}$ within each {hkl} plane perpendicular to the direction vector $\vec{a} = \langle hkl \rangle$. See Fig. 1 for a description of the relationship between $\vec{a}$, b, and χ.

with anodes based on K, the most compliant metal examined. The slightly stiffer anti-perovskites are in principle suitable for use with any of the alkaline metal anodes (Li, Na, and K). NASICON-type and garnet electrolytes expand this window beyond the alkali metals to include MV anodes such as Ca and Mg. Finally, the perovskites, which are the stiffest SE overall, are projected to be compatible with all of the anode materials examined here, with the exception of Si.

Conclusions

First-principles calculations were employed to calculate the elastic constants and aggregate, polycrystalline elastic properties of several anode materials of relevance for battery applications: Al, Ca, Li, Na, K, Mg, Zn, and Si. It is demonstrated that careful sampling of reciprocal space is required to converge the elastic constants. Direction-dependent elastic properties were derived from the stiffness tensors, and the effect of temperature on these properties was evaluated using the quasi-harmonic approximation. In general, excellent agreement between the present calculations and experimental measurements of the elastic constants and polycrystalline elastic moduli is obtained.

The elastic properties were mapped as a function of crystallographic direction. For cubic materials under axial loading, the stiffest (most compliant) orientation is $\langle 111 \rangle$ ($\langle 100 \rangle$), while in shear $\langle 100 \rangle$ ($\langle 111 \rangle$) is the stiffest (most compliant). The alkali metals are predicted to be the softest, growing softer with increasing atomic number. These systems are also the most anisotropic, with the degree of anisotropy increasing with increasing temperature. In contrast, multivalent Al and Mg are the most isotropic; nevertheless, their elastic properties are the most sensitive to temperature among the elements studied here. As expected, Si, the only non-metal, is the stiffest overall.

These data demonstrate that the maximum anisotropic shear modulus of some metals can be more than twice as large as their averaged or polycrystalline shear modulus. Hence, in the context of Monroe and Newman's theory of dendrite initiation, *anisotropic* elastic behavior, and not *average* behavior, may be an important factor in rationalizing the relative tendencies of different anode compositions to form dendrites during electrodeposition. The viability of several SE classes for use in conjunction with a given anode was projected by comparing the SE shear modulus with twice the maximum resolved shear modulus of the associated anode at 300 K.

In addition to providing insight into dendrite initiation for several combinations of anodes and solid electrolytes, the elastic properties data presented here will be of value as input to more detailed models of mechano-electrochemical behavior at anode/solid electrolyte interfaces.

Acknowledgments

The authors acknowledge financial support from the U.S. National Science Foundation, grant CBET-1351482.

ORCID

Donald J. Siegel https://orcid.org/0000-0001-7913-2513

References

1. R. van Noorden, "The rechargeable revolution: a better battery." *Nature*, **507**, 26 (2014).
2. M. Armand and J. M. Tarascon, "Building better batteries." *Nature*, **451**, 652 (2008).
3. G. Crabtree, "The joint center for energy storage research: a new paradigm for battery research and development." *AIP Conf. Proc.*, **1652**, 112 (2015).
4. J. W. Choi and D. Aurbach, "Promise and reality of post-Lithium-Ion batteries with high energy densities." *Nat. Rev. Mater.*, **1**, 1 (2016).
5. H. Kim, G. Jeong, Y. U. Kim, J. H. Kim, C. M. Park, and H. J. Sohn, "Metallic anodes for next generation secondary batteries." *Chem. Soc. Rev.*, **42**, 9011 (2013).
6. K. Brandt, "Historical development of secondary lithium batteries." *Solid State Ionics*, **69**, 173 (1994).
7. Y. Li and H. Dai, "Recent advances in Zinc-Air batteries." *Chem. Soc. Rev.*, **43**, 5257 (2014).
8. D. Kundu, B. D. Adams, V. Duffort, S. H. Vajargah, and L. F. Nazar, "A high-capacity and long-life aqueous rechargeable Zinc battery using a metal oxide intercalation cathode." *Nat. Energy*, **1**, 1 (2016).
9. J. Deng, W.-B. Luo, S.-L. Chou, H.-K. Liu, and S.-X. Dou, "Sodium-Ion batteries: from academic research to practical commercialization." *Adv. Energy Mater.*, **8**, 1701428 (2018).
10. P. Hartmann, C. L. Bender, M. Vracar, A. K. Durr, A. Garsuch, J. Janek, and P. Adelhelm, "A rechargeable room-temperature sodium superoxide (NaO_2) battery." *Nat. Mater.*, **12**, 228 (2013).
11. A. Manthiram and X. Yu, "Ambient temperature sodium-sulfur batteries." *Small*, **11**, 2108 (2015).
12. X. Ren and Y. Wu, "A low-overpotential potassium-oxygen battery based on potassium superoxide." *J. Am. Chem. Soc.*, **135**, 2923 (2013).
13. Q. Zhao, Y. Hu, K. Zhang, and J. Chen, "Potassium-sulfur batteries: a new member of room-temperature rechargeable metal-sulfur batteries." *Inorg. Chem.*, **53**, 9000 (2014).
14. T. Jiang, M. J. C. Brym, G. Dube, A. Lasia, and G. M. Brisard, "Electrodeposition of Aluminium from Ionic Liquids: Part II—studies on the electrodeposition of Aluminum from Aluminum Chloride (AlCl(3))—Trimethylphenylammonium Chloride (TMPAC) Ionic Liquids." *Surf. Coat. Technol.*, **201**, 10 (2006).
15. Q. Li and N. J. Bjerrum, "Aluminum as anode for energy storage and conversion: a review." *J. Power Sources*, **110**, 1 (2002).
16. M. C. Lin et al., "An ultrafast rechargeable Aluminium-Ion battery." *Nature*, **520**, 325 (2015).
17. D. Aurbach, R. Skaletsky, and Y. Gofer, "The electrochemical behavior of calcium electrodes in a few organic electrolytes." *J. Electrochem. Soc.*, **138**, 3536 (1991).
18. D. Wang, X. Gao, Y. Chen, L. Jin, C. Kuss, and P. G. Bruce, "Plating and stripping calcium in an organic electrolyte." *Nat. Mater.*, **17**, 16 (2018).
19. M. Matsui, "Study on electrochemically deposited Mg metal." *J. Power Sources*, **196**, 7048 (2011).
20. R. Davidson et al., "Formation of magnesium dendrites during electrodeposition." *ACS Energy Lett.*, **4**, 375 (2018).
21. T. Hirai, I. Yoshimatsu, and J. Yamaki, "Influence of electrolyte on lithium cycling efficiency with pressurized electrode stack." *J. Electrochem. Soc.*, **141**, 611 (1994).
22. C. Monroe and J. Newman, "The impact of elastic deformation on deposition kinetics at lithium polymer interfaces." *J. Electrochem. Soc.*, **152**, A396 (2005).
23. K. Ishiguro, Y. Nakata, M. Matsui, I. Uechi, Y. Takeda, O. Yamamoto, and N. Imanishi, "Stability of Nb-doped cubic Li7La3Zr2O12 with Lithium metal." *J. Electrochem. Soc.*, **160**, A1690 (2013).
24. M. Nagao, A. Hayashi, M. Tatsumisago, T. Kanetsuku, T. Tsuda, and S. Kuwabata, "In situ SEM study of a lithium deposition and dissolution mechanism in a Bulk-Type solid-state cell with a Li2S-P2S5 solid electrolyte." *Phys. Chem. Chem. Phys.*, **15**, 18600 (2013).
25. K. Ishiguro, H. Nemori, S. Sunahiro, Y. Nakata, R. Sudo, M. Matsui, Y. Takeda, O. Yamamoto, and N. Imanishi, "Ta-doped Li7La3Zr2O12 for water-stable lithium electrode of Lithium-Air batteries." *J. Electrochem. Soc.*, **161**, A668 (2014).
26. R. Sudo, Y. Nakata, K. Ishiguro, M. Matsui, A. Hirano, Y. Takeda, O. Yamamoto, and N. Imanishi, "Interface behavior between garnet-type lithium-conducting solid electrolyte and lithium metal." *Solid State Ionics*, **262**, 151 (2014).
27. Y. Ren, Y. Shen, Y. Lin, and C.-W. Nan, "Direct observation of lithium dendrites inside garnet-type Lithium-Ion solid electrolyte." *Electrochem. Comm.*, **57**, 27 (2015).
28. E. J. Cheng, A. Sharafi, and J. Sakamoto, "Intergranular Li metal propagation through polycrystalline Li6.25Al0.25La3Zr2O12 ceramic electrolyte." *Electrochim. Acta*, **223**, 85 (2017).
29. B. Wu, S. Wang, J. Lochala, D. Desrochers, B. Liu, W. Zhang, J. Yang, and J. Xiao, "The role of the solid electrolyte interphase layer in preventing Li dendrite growth in solid-state batteries." *Energy Environ. Sci.*, **11**, 1803 (2018).
30. L. Porz, T. Swamy, B. W. Sheldon, D. Rettenwander, T. Frömling, H. L. Thaman, S. Berendts, R. Uecker, W. C. Carter, and Y.-M. Chiang, "Mechanism of lithium metal penetration through inorganic solid electrolytes." *Adv. Energy Mater.*, **7**, 1701003 (2017).
31. P. Barai, K. Higa, and V. Srinivasan, "Lithium dendrite growth mechanisms in polymer electrolytes and prevention strategies." *Phys. Chem. Chem. Phys.*, **19**, 20493 (2017).
32. P. Barai, K. Higa, and V. Srinivasan, "Impact of external pressure and electrolyte transport properties on Lithium dendrite growth." *J. Electrochem. Soc.*, **165**, A2654 (2018).
33. J. R. Greer and W. D. Nix, "Size dependence of mechanical properties of gold at the Sub-Micron scale." *Appl. Phys. A: Solids Surf.*, **80**, 1625 (2005).
34. J. R. Greer and W. D. Nix, "Nanoscale gold pillars strengthened through dislocation starvation." *Phys. Rev. B*, **73**, 1 (2006).
35. J.-Y. Kim and J. R. Greer, "Tensile and compressive behavior of gold and molybdenum single crystals at the nano-scale." *Acta Mater.*, **57**, 5245 (2009).
36. C. M. Byer, B. Li, B. Cao, and K. T. Ramesh, "Microcompression of single-crystal magnesium." *Scr. Mater.*, **62**, 536 (2010).
37. Q. Yu, Z. W. Shan, J. Li, X. Huang, L. Xiao, J. Sun, and E. Ma, "Strong crystal size effect on deformation twinning." *Nature*, **463**, 335 (2010).
38. C. Xu, Z. Ahmad, A. Aryanfar, V. Viswanathan, and J. R. Greer, "Enhanced strength and temperature dependence of mechanical properties of Li at small scales and its implications for Li metal anodes." *Proc. Natl Acad. Sci. USA*, **114**, 57 (2017).
39. J. R. Greer and J. T. M. De Hosson, "Plasticity in small-sized metallic systems: intrinsic vs extrinsic size effect." *Prog. Mater Sci.*, **56**, 654 (2011).
40. G. Li and C. W. Monroe, "Dendrite nucleation in Lithium-conductive ceramics." *Phys. Chem. Chem. Phys.*, **21**, 20354 (2019).
41. E. G. Herbert, N. J. Dudney, M. Rochow, V. Thole, and S. A. Hackney, "On the mechanisms of stress relaxation and intensification at the Lithium/Solid-State electrolyte interface." *J. Mater. Res.*, **34**, 3593 (2019).
42. W. S. LePage, Y. Chen, E. Kazyak, K.-H. Chen, A. J. Sanchez, A. Poli, E. M. Arruda, M. D. Thouless, and N. P. Dasgupta, "Lithium mechanics: roles of strain rate and temperature and implications for Lithium metal batteries." *J. Electrochem. Soc.*, **166**, A89 (2019).
43. A. Masias, N. Felten, R. Garcia-Mendez, J. Wolfenstine, and J. Sakamoto, "Elastic, plastic, and creep mechanical properties of Lithium metal." *J. Mater. Sci.*, **54**, 2585 (2018).
44. S. Yu and D. J. Siegel, "Grain boundary softening: a potential mechanism for Lithium metal penetration through stiff solid electrolytes." *ACS Appl. Mater. Interfaces*, **10**, 38151 (2018).
45. Y. Wang, J. J. Wang, H. Zhang, V. R. Manga, S. L. Shang, L. Q. Chen, and Z. K. Liu, "A first-principles approach to finite temperature elastic constants." *J. Phys. Condens. Matter*, **22**, 225404 (2010).
46. J. M. Wills, O. Eriksson, P. Soderlind, and A. M. Boring, "Trends of the elastic constants of cubic transition metals." *Phys. Rev. Lett.*, **68**, 2802 (1992).
47. M. E. Fine, L. D. Brown, and H. L. Marcus, "Elastic constants vs melting temperature in metals." *Scr. Metall.*, **18**, 951 (1984).
48. M. J. Mehl and L. L. Boyer, "Calculation of energy barriers for physically allowed lattice-invariant strains in aluminum and iridium." *Phys. Rev. B: Condens. Matter Mater. Phys.*, **43**, 9498 (1991).
49. L. L. Boyer, E. Kaxiras, M. J. Mehl, J. L. Feldman, and J. Q. Broughton, "Application of magic strains to predict new ordered phases: a Five-Fold coordinated crystal structure for silicon." *Ordering and Disordering in Alloys*, ed. A. R. Yavari (Springer Netherlands, Dordrecht) p. 506 (1992).
50. M. J. Mehl, J. E. Osburn, D. A. Papaconstantopoulos, and B. M. Klein, "Structural properties of ordered High-Melting-temperature intermetallic alloys from First-Principles Total-Energy calculations." *Phys. Rev. B: Condens. Matter Mater. Phys.*, **41**, 10311 (1990).
51. J. E. Osburn, M. J. Mehl, and B. M. Klein, "First-principles calculation of the elastic moduli of Ni3Al." *Phys. Rev. B: Condens. Matter Mater. Phys.*, **43**, 1805 (1991).
52. W. Kohn and L. J. Sham, "Self-consistent equations including exchange and correlation effects." *Phys. Rev.*, **140**, A1133 (1965).
53. G. Kresse and J. Hafner, "Ab-initio molecular-dynamics for liquid-metals." *Phys. Rev. B*, **47**, 558 (1993).
54. G. Kresse and J. Hafner, "Norm-conserving and ultrasoft pseudopotentials for First-Row and transition element." *J. Phys. Condens. Matter*, **6**, 8245 (1994).
55. G. Kresse and J. Furthmuller, "Efficiency of ab-initio total energy calculations for metals and semiconductors using a Plane-Wave basis set." *Comput. Mater. Sci.*, **6**, 15 (1996).
56. G. Kresse and J. Furthmuller, "Efficient iterative schemes for ab-initio total-energy calculations using a Plane-Wave basis set." *Phys. Rev. B*, **54**, 11169 (1996).
57. P. E. Blöchl, "Projector augmented-wave method." *Phys. Rev. B*, **50**, 17953 (1994).
58. M. Methfessel and A. T. Paxton, "High-precision sampling for Brillouin-Zone integration in metals." *Phys. Rev. B*, **40**, 3616 (1989).
59. M. de Jong et al., "Charting the complete elastic properties of inorganic crystalline compounds." *Sci. Data*, **2**, 150009 (2015).
60. M. de Jong et al., "Data from: charting the complete elastic properties of inorganic crystalline compounds." *Charting the Complete Elastic Properties of Inorganic Crystalline Compounds*, ed. D. D. Repository (Dryad, Dryad) (2015).
61. J. P. Perdew, K. Burke, and M. Ernzerhof, "Generalized gradient approximation made simple." *Phys. Rev. Lett.*, **77**, 3865 (1996).
62. Y. Le Page and P. Saxe, "Symmetry-general least-squares extraction of elastic data for strained materials from ab-initio calculations of stress." *Phys. Rev. B*, **65**, 104104 (2002).
63. J. F. Nye, *Physical Properties of Crystals: Their Representation by Tensors and Matrices.* (Oxford University Press, Oxford) (1957).
64. R. Hill, "The elastic behaviour of a crystalline aggregate." *Proc. Phys. Soc. London, Sect. A*, **65**, 349 (1952).
65. S. I. Ranganathan and M. Ostoja-Starzewski, "Universal elastic anisotropy index." *Phys. Rev. Lett.*, **101**, 055504 (2008).

66. A. Marmier, Z. A. D. Lethbridge, R. I. Walton, C. W. Smith, S. C. Parker, and K. E. Evans, "ElAM: a computer program for the analysis and representation of anisotropic elastic properties." *Comput. Phys. Commun.*, **181**, 2102 (2010).
67. A. Togo, L. Chaput, I. Tanaka, and G. Hug, "First-principles phonon calculations of thermal expansion in Ti3SiC2, Ti3AlC2, and Ti3GeC2." *Phys. Rev. B*, **81**, 174301 (2010).
68. A. Togo, F. Oba, and I. Tanaka, "First-principles calculations of the ferroelastic transition between rutile-type and CaCl2-Type SiO_2 at high pressures." *Phys. Rev. B*, **78**, 134106 (2008).
69. A. Jain et al., "Commentary: the materials project: a materials genome approach to accelerating materials innovation." *APL Mater.*, **1**, 011002 (2013).
70. M. Born and K. Huang, *Dynamical Theory of Crystal Lattices.* (Oxford University Press, Oxford) (1954).
71. Y. P. Varshni, "Temperature dependence of the elastic constants." *Phys. Rev. B*, **2**, 3952 (1970).
72. N. P. Balsara, M. Singh, H. B. Eitouni, and E. D. Gomez, "High elastic modulus polymer electrolytes." U.S. Pat. 8563168 B2 (2013).
73. M. B. Satterfield, P. W. Majsztrik, H. Ota, J. B. Benziger, and A. B. Bocarsly, "Mechanical properties of Nafion and Titania/Nafion composite membranes for polymer electrolyte membrane fuel cells." *J. Polym. Sci., Part B: Polym. Phys.*, **44**, 2327 (2006).
74. A. Sakuda, A. Hayashi, and M. Tatsumisago, "Sulfide solid electrolyte with favorable mechanical property for All-Solid-state lithium battery." *Sci. Rep.*, **3**, 1 (2013).
75. Y. Yang, Q. Wu, Y. Cui, Y. Chen, S. Shi, R. Z. Wang, and H. Yan, "Elastic properties, defect thermodynamics, electrochemical window, phase stability, and Li (+) Mobility of Li3PS4: insights from first-principles calculations." *ACS Appl. Mater. Interfaces*, **8**, 25229 (2016).
76. Z. Deng, Z. Wang, I.-H. Chu, J. Luo, and S. P. Ong, "Elastic properties of alkali superionic conductor electrolytes from first principles calculations." *J. Electrochem. Soc.*, **163**, A67 (2016).
77. E. G. Herbert, W. E. Tenhaeff, N. J. Dudney, and G. M. Pharr, "Mechanical characterization of LiPON films using nanoindentation." *Thin Solid Films*, **520**, 413 (2011).
78. K. Kim and D. J. Siegel, "Correlating lattice distortions, ion migration barriers, and stability in solid electrolytes." *J. Mater. Chem. A*, **7**, 3216 (2019).
79. J. Wolfenstine, J. L. Allen, J. Sakamoto, D. J. Siegel, and H. Choe, "Mechanical behavior of Li-Ion-conducting crystalline oxide-based solid electrolytes: a brief review." *Ionics*, **24**, 1271 (2018).
80. S. Yu, R. D. Schmidt, R. Garcia-Mendez, E. Herbert, N. J. Dudney, J. B. Wolfenstine, J. Sakamoto, and D. J. Siegel, "Elastic properties of the solid electrolyte Li7La3Zr2O12 (LLZO)." *Chem. Mater.*, **28**, 197 (2016).
81. H. M. Ledbetter, "Elastic properties of Zinc—Compilation and a review." *J. Phys. Chem. Ref. Data*, **6**, 1181 (1977).
82. J. Turley and G. Sines, "The anisotropy of Young's modulus, Shear Modulus and Poisson's Ratio in cubic materials." *J. Phys. D: Appl. Phys.*, **4**, 264 (1971).